An X-Ray and Radio View of the 2022 Reactivation of the Magnetar SGR J1935+2154

A. Y. Ibrahim[1,2] , A. Borghese[3,4] , F. Coti Zelati[1,2] , E. Parent[1,2] , A. Marino[1,2] , O. S. Ould-Boukattine[5,6] , N. Rea[1,2] ,
S. Ascenzi[7,8,9] , D. P. Pacholski[10,11] , S. Mereghetti[10] , G. L. Israel[12] , A. Tiengo[10,13] , A. Possenti[14] , M. Burgay[14] ,
R. Turolla[15,16] , S. Zane[16] , P. Esposito[10,13] , D. Götz[17] , S. Campana[18] , F. Kirsten[19] , M. P. Gawroński[20] , and
J. W. T. Hessels[5,6]

[1] Institute of Space Sciences (ICE, CSIC), Campus UAB, Carrer de Can Magrans s/n, E-08193 Barcelona, Spain; ibrahim@ice.csic.es
[2] Institut d'Estudis Espacials de Catalunya (IEEC), E-08860 Castelldefels (Barcelona), Spain
[3] Instituto de Astrofísica de Canarias, E-38205 La Laguna, Tenerife, Spain
[4] Departamento de Astrofísica, Universidad de La Laguna, E-38206 La Laguna, Tenerife, Spain
[5] ASTRON, Netherlands Institute for Radio Astronomy, Oude Hoogeveensedijk 4, 7991 PD Dwingeloo, The Netherlands
[6] Anton Pannekoek Institute for Astronomy, University of Amsterdam, Science Park 904, 1098 XH Amsterdam, The Netherlands
[7] Gran Sasso Science Institute, Viale F. Crispi 7, I-67100 L'Aquila (AQ), Italy
[8] INFN—Laboratori Nazionali Del Gran Sasso, I-67100 L'Aquila (AQ), Italy
[9] INAF—Osservatorio Astronomico di Brera, via E. Bianchi 46, 23807, Merate (LC), Italy
[10] INAF—Istituto di Astrofisica Spaziale e Fisica Cosmica di Milano, via A. Corti 12, I-20133 Milano, Italy
[11] Dipartimento di Fisica G. Occhialini, Università degli Studi di Milano Bicocca, Piazza della Scienza 3, I-20126 Milano, Italy
[12] INAF—Osservatorio Astronomico di Roma, via Frascati 33, I-00078 Monteporzio Catone, Italy
[13] Scuola Universitaria Superiore IUSS Pavia, Palazzo del Broletto, piazza della Vittoria 15, I-27100 Pavia, Italy
[14] INAF—Osservatorio Astronomico di Cagliari, Via della Scienza 5, I-09047 Selargius, Italy
[15] Dipartimento di Fisica e Astronomia "Galileo Galilei," Università di Padova, via F. Marzolo 8, I-35131 Padova, Italy
[16] Mullard Space Science Laboratory, University College London, Holmbury St. Mary, Dorking, Surrey, RH5 6NT, UK
[17] AIM-CEA/DRF/Irfu/Département d'Astrophysique, CNRS, Université Paris-Saclay, Université de Paris Cité, Orme des Merisiers, F-91191 Gif-sur-Yvette, France
[18] INAF—Osservatorio Astronomico di Brera, Via Bianchi 46, Merate (LC), I-23807, Italy
[19] Department of Space, Earth and Environment, Chalmers University of Technology, Onsala Space Observatory, 439 92, Onsala, Sweden
[20] Institute of Astronomy, Faculty of Physics, Astronomy and Informatics, Nicolaus Copernicus University, Grudziadzka 5, 87-100 Toruń, Poland

Abstract

Recently, the Galactic magnetar SGR J1935+2154 has garnered attention due to its emission of an extremely luminous radio burst, reminiscent of fast radio bursts (FRBs). SGR J1935+2154 is one of the most active magnetars, displaying flaring events nearly every year, including outbursts as well as short and intermediate bursts. Here, we present our results on the properties of the persistent and bursting X-ray emission from SGR J1935+2154 during the initial weeks following its outburst on 2022 October 10. The source was observed with XMM-Newton and NuSTAR (quasi-)simultaneously during two epochs, separated by ∼5 days. The persistent emission spectrum is well described by an absorbed blackbody plus power-law model up to an energy of ∼25 keV. No significant changes were observed in the blackbody temperature ($kT_{\rm BB} \sim$ 0.4 keV) and emitting radius ($R_{\rm BB} \sim$ 1.9 km) between the two epochs. However, we observed a slight variation in the power-law parameters. Moreover, we detected X-ray pulsations in all the data sets and derived a spin-period derivative of $\dot{P} = 5.52(5) \times 10^{-11}$ s s^{-1}. This is 3.8 times larger than the value measured after the first recorded outburst in 2014. Additionally, we performed quasi-simultaneous radio observations using three 25–32 m class radio telescopes for a total of 92.5 hr to search for FRB-like radio bursts and pulsed emission. However, our analysis did not reveal any radio bursts or periodic emission.

1. Introduction

Magnetars are a subgroup of isolated neutron stars with ultra-high magnetic fields of $B \approx 10^{14}$–10^{15} G, whose decay and instability are believed to be the main energy source of their emission (Duncan & Thompson 1992). Magnetars have spin periods P that range between 0.3 and 12 s and large spin-down rates between $\dot{P} \sim 10^{-13}$ and 10^{-11} s s^{-1}, although magnetar-like emission has also been detected from peculiar pulsars that may not necessarily have P and $\dot{P}$ falling within the aforementioned range (e.g., Rea et al. 2010; Archibald et al. 2016; Rea et al. 2016). Magnetars are persistent X-ray sources with luminosities of $L_X \approx 10^{31}$–10^{36} erg s^{-1} (for reviews see, e.g., Turolla et al. 2015; Kaspi & Beloborodov 2017; Esposito et al. 2021). In addition, they are characterized by transient activities, which may affect the spectral and timing properties of the persistent emission. Based on their duration, these activities can be divided into short- and long-lived events. The former include bursts of tens/hundreds of milliseconds duration and giant flares lasting up to a few minutes, and reaching peak luminosities as high as 10^{47} erg s^{-1}. The latter, known as outbursts, are sudden increases of the persistent X-ray flux by a factor of 10–1000, followed by a gradual decay over a period of months to years (see, e.g., the Magnetar Outburst Online Catalog; Coti Zelati et al. 2018).[21]

---

[21] http://magnetars.ice.csic.es/

On 2014 July 5, the Burst Alert Telescope (BAT) on board the Neil Gehrels Swift Observatory (Swift; Gehrels et al. 2004) detected a short burst, leading to the discovery of a new magnetar, SGR J1935+2154 (hereafter SGR J1935; Stamatikos et al. 2014). Follow-up observations enabled the measurement of the source spin period $P \sim 3.24$ s and spin-down rate of $\dot{P} \sim 1.43 \times 10^{-11}$ s s^{-1}. These values resulted in a surface dipolar magnetic field $B \sim 2.2 \times 10^{14}$ G at the equator, confirming the magnetar nature of the source (Israel et al. 2016). The distance to the magnetar has been the focus of various works. Some of these studies associate SGR J1935 with the supernova remnant G57.2+0.8, for which distances of 6.6 ± 0.7 kpc (Zhou et al. 2020) and $\leqslant 10$ kpc (Kozlova et al. 2016) have been derived. On the other hand, other studies reported a distance of $4.4^{+2.8}_{-1.3}$ kpc, based on the analysis of an expanding dust-scattering ring associated with a bright X-ray burst (Mereghetti et al. 2020).

Since its discovery, SGR J1935 has been a very active source, experiencing multiple outbursts in 2015, 2016 (twice), and 2020 (see, e.g., Younes et al. 2017; Borghese et al. 2020), as well as frequent bursting episodes (e.g., Lin et al. 2020). Additionally, one day after the 2020 reactivation, a short and very bright, double-peaked radio burst (known as FRB 200428) temporally coincident with a hard X-ray burst was observed (Bochenek et al. 2020; CHIME/FRB Collaboration et al. 2020; Mereghetti et al. 2020; Li et al. 2021; Ridnaia et al. 2021; Tavani et al. 2021). This was the first time SGR J1935 was detected in the radio band. The radio burst showed properties similar to those of fast radio bursts (FRBs), providing strong evidence that magnetars may power at least a subgroup of FRBs.

On 2022 October 10–11, multiple short X-ray bursts were detected from SGR J1935 by INTEGRAL, Swift/BAT, and other X-ray satellites indicating a reactivation of the source (e.g., Ibrahim et al. 2022; Mereghetti et al. 2022; Palmer 2022). Following this bursting activity, NICER began observing the source and measured a persistent X-ray flux that was about one order of magnitude higher than the quiescent level (Younes et al. 2022b). A new outburst had begun. Similarly to the 2020 outburst, radio bursts with X-ray counterparts were also observed during the initial stage of this outburst (e.g., Younes et al. 2022a; Maan et al. 2022; Pearlman & Chime/FRB Collaboration 2022), but none as bright as FRB 200428.

Here, we report on the X-ray persistent and bursting emission properties of SGR J1935 during the first weeks of the most recent active period, as well as on our searches for single pulses and pulsed emission in quasi-simultaneous radio observations. We first summarize the X-ray data analysis procedure in Section 2. We then present the timing and spectral analysis, as well as a search for short bursts in Section 3. In Section 4, we describe our radio observations. Finally, Section 5 presents a discussion of our findings.

2. X-Ray Observations and Data Reduction

We report on nearly simultaneous XMM-Newton and NuSTAR observations, carried out between 2022 October 15 and 22. Data reduction was carried out using the HEASOFT package v6.31 (NASA High Energy Astrophysics Science Archive Research Center 2014) and the Science Analysis Software v.19.1.0 (SAS; Gabriel et al. 2004) with the latest calibration files.[22]

---

[22] https://www.cosmos.esa.int/web/xmm-newton/sas

Throughout this work, we adopted the coordinates reported by Israel et al. (2016), i.e., R.A. = 19^{h}34^{m}55^{s}598, decl. = +21° 53'47".79 (J2000.0), and the JPL planetary ephemeris DE 200 to convert the photon arrival times to the solar system barycenter. Additionally, to be consistent with our previous works (e.g., Borghese et al. 2022), we adopted a distance of 6.6 kpc (Zhou et al. 2020) and quote all uncertainties at a 1σ confidence level.

2.1. XMM-Newton

XMM-Newton observed SGR J1935 twice with the European Photon Imaging Camera (EPIC), for an exposure time of ~ 40 and ~ 50 ks for the first (ID:0902334101, between 2022 October 15 19:48:48 UTC, and October 16 12:06:17 UTC) and the second (ID:0882184001, 2022 October 22 between 03:22:56 and 22:12:09 UTC) observations, respectively. For each observation, the EPIC-pn (Strüder et al. 2001) was set in Small Window mode (time resolution of 5.7 ms) while the EPIC-MOS1 and EPIC-MOS2 (Turner et al. 2001) were set in Full Window mode (time resolution of 2.6 s) and Timing mode (time resolution of 1.75 ms), respectively. Following standard procedures, we filtered the event files for periods of high background activity, resulting in a net exposure of 39 and 41 ks for the first and the second pointings. No pile-up was detected. The source counts were extracted from a circle of radius 30" centered on the source and the background level was estimated from a 60" radius circle far from the source, on the same CCD. In this study, our primary focus was on data collected with the EPIC-pn, because of its higher counting statistics owing to its larger effective area compared to that of the two MOSs. However, we verified that the MOS data yielded consistent results.

2.2. NuSTAR

SGR J1935 was observed twice with NuSTAR (Harrison et al. 2013): the first time between 2022 October 18 21:51:09 UTC, and October 20 22:21:09 UTC (ID:80702311002, on-source exposure time ~ 50 ks); the second time between 2022 October 22 22:21:09 UTC, and October 24 03:11:09 UTC (ID:80702311004, on-source exposure time ~ 51 ks). Source photons were accumulated within a circular region of radius 100". A similar region centered on a position uncontaminated by the source emission was used for the extraction of the background events. The light curves, the spectra, and the corresponding response files for the two focal-plane detectors, referred to as FPMA and FPMB, were extracted using the NUPRODUCTS script.

2.3. INTEGRAL

We searched the INTEGRAL archive for data obtained simultaneously with XMM-Newton and NuSTAR observations. This resulted in 23 pointings where SGR J1935 was in the field of view of the IBIS coded-mask imaging instrument. These pointings cover about 60% of the first XMM-Newton observation (from October 15 at 18:51 to October 16 at 04:47 UTC) and 15% of the first NuSTAR observation (on October 19, from 14:43 to 17:45 UTC). We used data from the IBIS/ISGRI detector that operates in the nominal energy range 15–1000 keV, providing photon-by-photon data with an excellent time resolution of 73 μs. INTEGRAL data were only examined for the presence of short bursts.
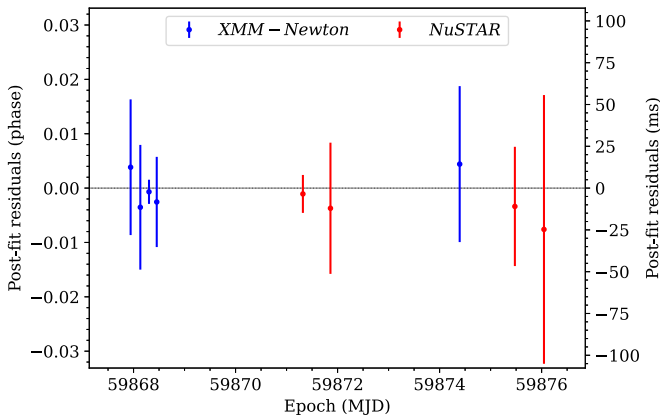
Figure 1. Post-fit residuals of our best-fit coherent timing solution for SGR J1935 (Table 1).

3. X-Ray Analysis and Results

3.1. X-Ray Timing Analysis

To perform the timing analysis of SGR J1935, we first filtered out the burst events from the data set so that they do not affect the integrated pulse profile morphology. We then used the `photonphase` task of the `PINT` software (Luo et al. 2021) to assign a rotational phase to the barycentered events by extrapolating the ephemeris from Borghese et al. (2022). In order to use the same fiducial reference phase for the XMM-Newton and NuSTAR data set, thus enabling phase coherence across the observations, only photons with energies below 15 keV were analyzed. We then combined those events into a stable template profile, which we modeled with multiple Gaussian components. Using the `photon_toa.py` tool of the `NICERsoft` package,[23] we extracted barycentric pulse time of arrivals (TOAs) and proceeded to phase-connect the four data set with the `TEMPO` timing software (Nice et al. 2015). We achieved coherence across the data set using a simple model that only has the spin frequency ν and its first derivative $\dot{\nu}$ as free parameters. We show the post-fit residuals in Figure 1 and provide our coherent solution in Table 1.

Using our timing model, we then computed the rotational phase associated with the (barycentric) XMM-Newton and NuSTAR burst epochs (Table A1). Figure 2 shows the burst phases against the integrated pulse profiles observed with both instruments. We find no evidence for a preferred burst rotational phase: the burst cumulative distribution in phase across a full rotation cycle is statistically consistent with a uniform distribution (we determined a p-value $> 25\%$ using both an Anderson–Darling and Kolmogorov–Smirnov test). Similarly, Younes et al. (2020) found no obvious clustering at any particular phase for the $\sim$220 bursts emitted from SGR J1935 during the 2020 reactivation.

Figure 3 shows the background-subtracted light curves folded using the timing solution presented in Table 1 as a function of energy for the two epochs. We modeled all the pulse profiles with a combination of a constant plus two sinusoidal functions, with periods fixed to those of the fundamental and first harmonic components. The pulse profile exhibits a simple morphology below 3 keV that evolves to a double-peaked shape at higher energies. At both epochs, the second peak (at phase $\sim$0.7) becomes more prominent above

---

[23] https://github.com/paulray/NICERsoft/wiki

Table 1
Coherent Timing Solution of SGR J1935 Derived from the XMM-Newton and NuSTAR Data

Parameter	Measured Value
R.A. (J2000)	19:34:55.598
decl. (J2000)	21:53:47.79
ν (s^{-1})	0.307525543(4)
$\dot{\nu}$ (10^{-12} s^{-2})	$-5.22(5)$
P (s)	3.25176241(5)
$\dot{P}$ (10^{-11})	5.52(5)
Epoch of frequency (MJD)	59871.00
Validity range (MJD)	59867.9–59876.0
Reference epoch (MJD)	59871.320339421679
Timescale	TDB
Solar system ephemeris	DE200
rms residuals (ms)	10.8
Daily-averaged rms residuals (ms)	8.1

	Derived Value
Surface dipolar magnetic field, B_{eq} (10^{14} G)	4.3
Spin-down luminosity, $\dot{E}$ (10^{34} erg s^{-1})	6.3
Characteristic age, τ_c (yr)	930

Note. Values in parentheses are the 1σ uncertainty in the last digit of the fitting parameters reported by `TEMPO`. The epoch of frequency refers to the reference time for the spin measurements at the solar system barycenter, while the reference epoch is the phase-zero reference for TOA phase predictions.

10 keV and dominates in the 25–79 keV energy interval. The separation between the two peaks increases with energy for both epochs from $\sim$0.3 to 0.35 in phase at soft X-rays ($<$10 keV) to $\sim$0.65–0.7 in phase at hard X-rays ($>$10 keV). Moreover, we detected a phase shift $\Delta\phi$ between the soft (0.3–10 keV) and hard (10–25 keV) energy bands. For the first peak, $\Delta\phi_{0.3-10/10-25}$ is 0.13 ± 0.02 cycles during the first epoch, with the hard photons anticipating the soft ones, and it is not significant for the second epoch. While for the second peak, we determined a shift of $\Delta\phi_{0.3-10/10-25} = 0.19 \pm 0.01$ and 0.22 ± 0.01 cycles for the first and second epochs, respectively, with the soft photons leading the hard ones. Finally, we studied the dependence of the pulsed fraction (PF) with the photon energy and its time evolution. The PF was computed by dividing the value of the semi-amplitude of the fundamental sinusoidal component describing the pulse profile by the average count rate. We did not detect any specific trend in the PF, apart from (i) an increase between the 10–25 keV and 25–79 keV bands for both epochs, and (ii) an increase of the 25–79 keV PF between the two epochs.

3.2. X-Ray Spectral Analysis of the Persistent Emission and Search for Diffuse Emission

The light curves of our observations exhibited several bursts, which will be properly investigated in Section 3.4. In order to exclude the bursts, we filtered out all the events with a count rate higher than the average count rate during the persistent state. We then used these filtered events to extract the spectra corresponding to the persistent emission only.

The spectral analysis was performed with XSPEC (v12.12.0; Arnaud 1996). We used `SPECGROUP` and `GRPPHA` tools to group the spectra with a minimum of 50 counts per energy bin for XMM-Newton/EPIC-pn and NuSTAR/FPMA data sets so as to use the χ^2 statistics. In the following fits, we only used
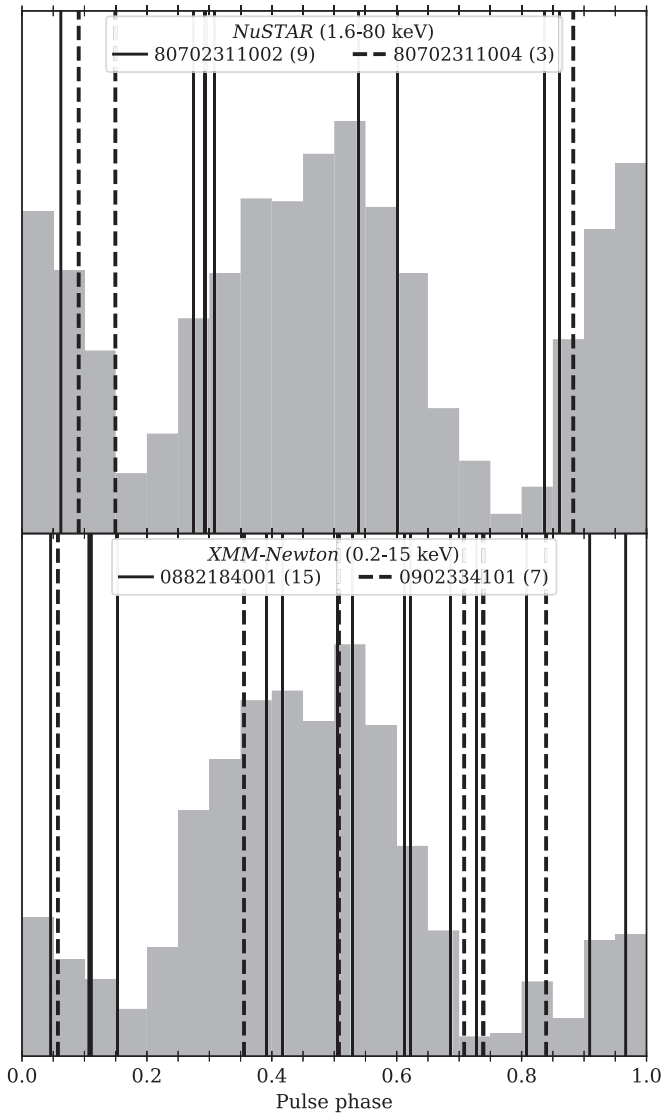
Figure 2. Phase distribution of the bursts (vertical black lines) detected in the NuSTAR (top) and XMM-Newton (bottom) data sets (Table A1), plotted against the combined pulse profiles in each data set (light gray) over one rotation cycle. The number of bursts in each observation is specified in parentheses next to the observation ID in the legends. The timing model of Table 1 was used for the absolute phase alignment. To show the burst phases more clearly, the burst widths (which have duty cycles ranging from ~1% to 16%) are not depicted in this figure.

NuSTAR/FPMA spectra, but checked that NuSTAR/FPMB gave consistent results. The XMM-Newton spectra were fit in the 0.5–10 keV energy interval, while for the NuSTAR ones the analysis was limited to the 3–25 keV energy band owing to the low signal-to-noise ratio (S/N) above 25 keV. We adopted the TBABS model with chemical abundances from Wilms et al. (2000) and photoionization cross sections from Verner et al. (1996) to describe the interstellar absorption.

We simultaneously fit the XMM-Newton and NuSTAR spectra with an absorbed blackbody plus power-law model (BB+PL), including a constant to account for cross-calibration between the two instruments (see Figure 4). N_H was tied up across all the four spectra, resulting in $N_H = (2.57 \pm 0.05) \times 10^{22}$ cm^{-2} (reduced chi-squared $\chi_\nu^2 = 1.08$ for 567 degrees of freedom, dof). This value is compatible with those derived in previous studies of

SGR J1935 (see, e.g., Younes et al. 2017). For each epoch (2022 October 15–18 and 22), we linked all the BB+PL parameters across the XMM-Newton and NuSTAR spectra. However, we allow these parameters to vary between the two epochs. Our analysis showed that there were no significant variations for the blackbody parameters between the first and second epochs, with an emitting radius of $R_{BB} \sim 1.9$ km and temperature of $kT_{BB} \sim 0.4$ keV. On the other hand, the photon index slightly changed from $\Gamma = 1.51 \pm 0.02$ to 1.41 ± 0.02 and the PL normalization decreased by a factor of ~1.5. The 0.5–25 keV observed fluxes were $(1.26 \pm 0.02) \times 10^{-11}$ and $(1.04 \pm 0.02) \times 10^{-11}$ erg cm^{-2} s^{-1}, giving luminosities of $(9.17 \pm 0.07) \times 10^{34}$ and $(7.48 \pm 0.07) \times 10^{34}$ erg s^{-1}. The PL component accounted for ~93% and ~89% of the total luminosity at the first and second epochs, respectively.

We also inspected the data taken from the EPIC-MOS1 detector for diffuse emission. For both epochs, we extracted radial profiles of the X-ray emission up to a distance of $100''$–$150''$ from the magnetar, both from the images covering the entire observation duration, and from the images covering variable time intervals following the detection of the brightest X-ray bursts (see Section 3.4 for more details). This second type of analysis was aimed at detecting short episodes of diffuse emission possibly associated with scattering haloes produced by the bursts. In no case did we find evidence of emission in excess of that from the magnetar.

3.3. Phase-resolved Spectroscopy

We performed a phase-resolved spectroscopy of the XMM-Newton and NuSTAR data sets of the magnetar persistent emission. Our aim is to investigate any changes with rotational phase (and time) of the parameters of the spectra corresponding to the two pulse profile peaks. Therefore, we extracted the 0.5–10 keV EPIC-pn and 3–25 keV FPMA spectra from the 0.0–0.5 (peak I) and 0.5–1.0 (peak II) phase intervals (see Figure 3).

The phase-resolved spectra were fit simultaneously with the BB+PL model. The column density was held fixed at the phase-averaged value ($N_H = 2.57 \times 10^{22}$ cm^{-2}; see Section 3.2). The spectral fitting results, reported in Table 2, revealed variations along the spin phase, which can be primarily attributed to fluctuations in the PL photon index. During the first epoch, the variability was more pronounced, with the index decreasing from 1.58 ± 0.04 for peak I to 1.36 ± 0.04 for peak II. In contrast, the second epoch displayed less variability, with the index slightly changing from 1.30 ± 0.04 (peak I) to 1.43 ± 0.04 (peak II). At a given epoch, the BB parameters are consistent with each other in the different phase ranges.

3.4. X-Ray Burst Search and Properties

We investigated the XMM-Newton and NuSTAR light curves of all observations for the presence of short bursts, applying the method described by Borghese et al. (2020; see also, e.g., Gavriil et al. 2004). We extracted time series with three different time resolutions (1/16, 1/32, and 1/64 s) in order to identify events of different durations. We classified a time bin as a burst if it had a probability $<10^{-4}(NN_{trials})^{-1}$ of being a Poissonian fluctuation of the average count rate, where N is the total number of time bins in a given light curve and N_{trials} is the number of timing resolutions used in the search.
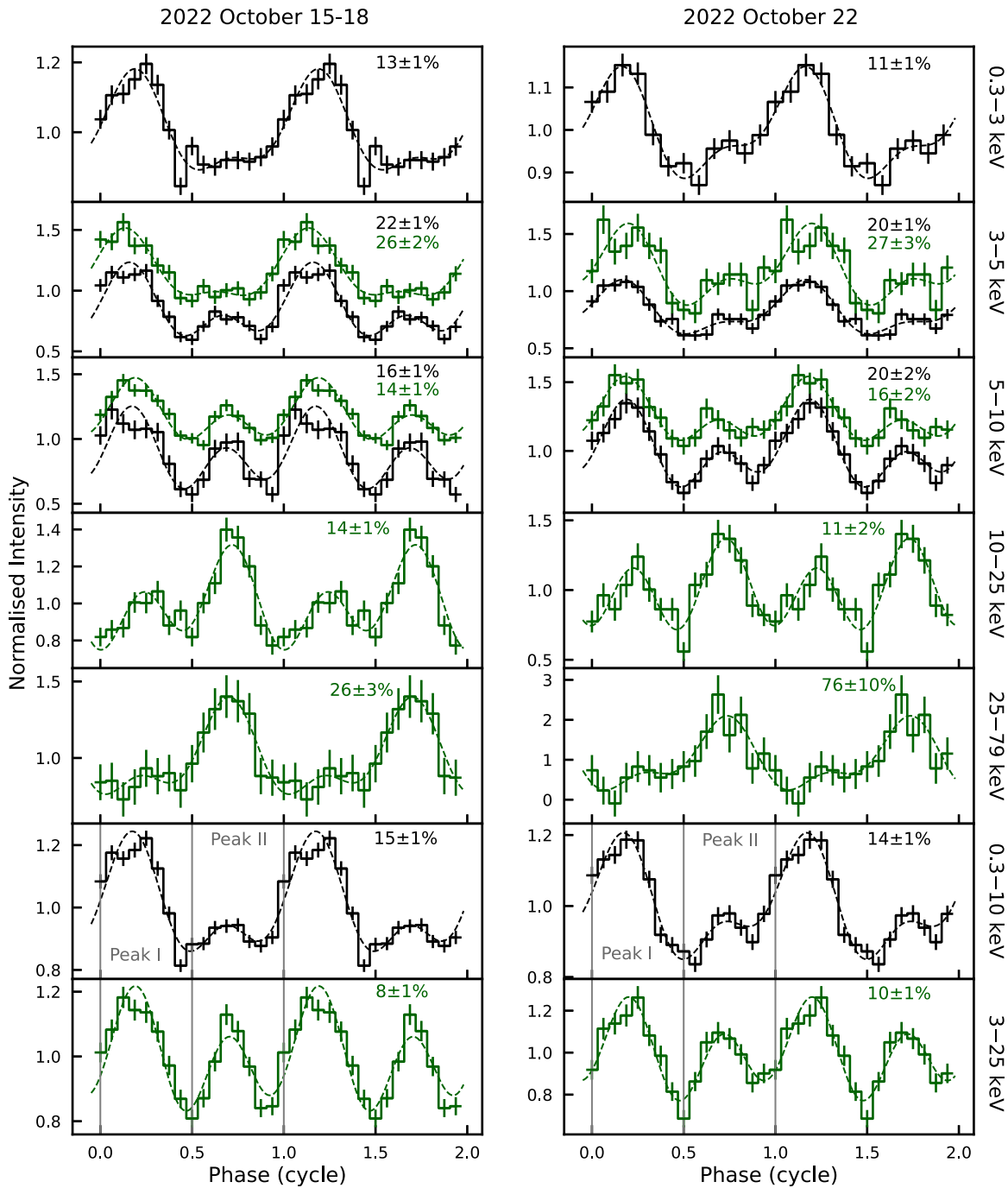
Figure 3. Background-subtracted, energy-resolved XMM-Newton/EPIC-pn (black) and NuSTAR/FPMA+FPMB (green) pulse profiles for the 2022 October 15–18 (left-hand panel) and October 22 (right-hand panel) data sets. The dashed line in each panel indicates the best fit for the profiles (for more details, see Section 3.1). The vertical gray lines in the last two panels denote the phase intervals adopted for the phase-resolved spectroscopy (for more details, see Section 3.3). The corresponding pulsed fraction values are reported in each panel. Two cycles are shown for clarity and some pulse profiles have been arbitrarily shifted along the *y*-axis.

We detected a total of 22 and 12 bursts in the XMM-Newton/ EPIC-pn and merged NuSTAR/FPMA+FPMB light curves, respectively. The burst epochs referred to the solar system barycenter, as well as the burst fluences and durations are reported in Table A1. Figure A1 shows the light curves for the two strongest bursts detected in XMM-Newton and NuS-TAR data.

We extracted the spectra for those events with at least 25 net counts for XMM-Newton and for the event with the highest counting statistics for NuSTAR (i.e., the burst labeled 80702311002 #9 in Table A1, with 80 net counts).

The background level was estimated from time intervals of the same duration in the persistent state. We employed a minimum number of counts to group the spectra that varies from burst to burst depending on the fluence of the burst itself. We applied the chi-squared statistic for model fitting, except for the cases where the counting statistic was too low. In such cases, we adopted the *W*-statistic instead. The spectra were fitted with an absorbed blackbody model, fixing N_H to the value obtained from the analysis of the phase-average broadband spectrum. The fit results are reported in Table A1.
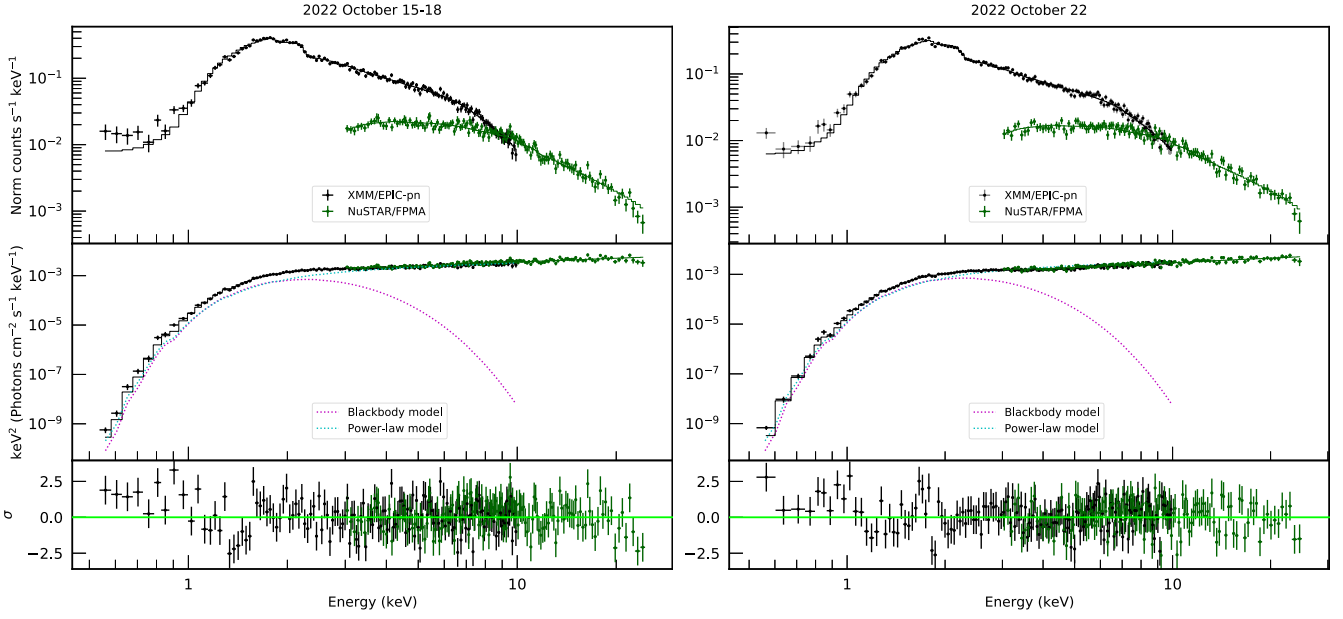
Figure 4. Spectra of the persistent emission of SGR J1935. The 0.5–10 keV XMM-Newton/EPIC-pn (black) and the 3–25 keV NuSTAR/FPMA (green) spectra are jointly fit with an absorbed blackbody plus power-law model. For each plot, the top panel shows the counts spectra and the best-fitting model; the middle panel shows the $E^2 f(E)$ unfolded spectra and the contribution of the single components (dotted lines); the bottom panel shows the post-fit residuals in units of standard deviations.

Table 2
Results of the Phase-resolved Spectral Analysis Presented in Section 3.3

	Phase	kT_{BB} (keV)	R_{BB} (km)	Γ	Flux[a] Unabs BB	Flux[a] Unabs PL
					$(10^{-12}$ erg cm^{-2} s$^{-1})$	
2022 October 15–18						
Peak I	0.0–0.5	0.42 ± 0.02	1.3 ± 0.1	1.58 ± 0.04	1.38 ± 0.02	7.36 ± 0.01
Peak II	0.5–1.0	0.44 ± 0.01	1.26 ± 0.08	1.36 ± 0.04	1.61 ± 0.02	7.19 ± 0.01
2022 October 22						
	Phase	kT_{BB} (keV)	R_{BB} (km)	Γ	Flux[a] Unabs BB	Flux[a] Unabs PL
					$(10^{-12}$ erg cm^{-2} s$^{-1})$	
Peak I	0.0–0.5	0.41 ± 0.01	1.86 ± 0.09	1.30 ± 0.04	2.52 ± 0.01	12.79 ± 0.01
Peak II	0.5–1.0	0.41 ± 0.01	1.83 ± 0.09	1.43 ± 0.04	2.38 ± 0.01	10.05 ± 0.01

Note.
[a] The fluxes are estimated in the 0.5–25 keV energy range.

Furthermore, for each observation, we extracted a stacked spectrum of all bursts and assigned the spectrum of the persistent-only emission as the background spectrum. We then fit the stacked spectra using the same model we adopted for the spectra of the single bursts (i.e., an absorbed blackbody with N_{H} fixed at 2.57×10^{22} cm^{-2}). The XMM-Newton spectra were well described by a single blackbody with a temperature of $kT_{\mathrm{BB}} = 1.14 \pm 0.06$ keV and $kT_{\mathrm{BB}} = 1.88 \pm 0.08$ keV for the first and second epochs, respectively. Using the assumed distance of SGR J1935, i.e., 6.6 kpc, we obtained radii of $R_{\mathrm{BB}} = 0.9 \pm 0.1$ km for the first epoch and $R_{\mathrm{BB}} = 1.14 \pm 0.07$ km for the second one. However, this model was unsatisfactory for the NuSTAR spectra, and thus a second blackbody component was added. This resulted in temperatures of $kT_{\mathrm{BB,cold}} = 0.5 \pm 0.2$ keV and $kT_{\mathrm{BB,hot}} = 3.1 \pm 0.3$ keV for the cold and hot components, respectively, with radii of $R_{\mathrm{BB,cold}} = 8^{+39}_{-3}$ km and $R_{\mathrm{BB,hot}} = 0.27^{+0.06}_{-0.04}$ km for the first epoch. For the second epoch, the temperatures were

$kT_{\mathrm{BB,cold}} = 0.8 \pm 0.3$ keV and $kT_{\mathrm{BB,hot}} = 4^{+4}_{-1}$ keV, with radii of $R_{\mathrm{BB,cold}} = 1.7^{+6.6}_{-0.5}$ km and $R_{\mathrm{BB,hot}} = 0.09 \pm 0.03$ km.

For the INTEGRAL data, the burst search was carried out in the 30–150 and 30–80 keV energy ranges, by examining light curves binned on seven timescales between 10 and 640 ms. Only the pixels that had more than 50% of their surface illuminated by the source were considered in our analysis. Potential bursts were identified as significant excesses above the expected background level derived from a running average. Once identified, these excesses were then examined through an imaging analysis to confirm their authenticity and positional association with the magnetar. This search resulted in the detection of only two bursts.

Among the three bursts seen with XMM-Newton during the INTEGRAL observations (i.e., the bursts labeled 0902334101 #1, #2, and #3 in Table A1), only the brightest one (#3) was detected by INTEGRAL as well. The burst had a fluence of 36.6 counts (30–150 keV) in ISGRI, over a duration

Table 3
Observational Setup of the Radio Telescopes

Station[a]	Band	Frequency Range (MHz)	Bandwidth[b] (MHz)	Bandwidth per Subband (MHz)	SEFD[c] (Jy)	Completeness[d] (Jy ms)	Time Observed (hr)
Wb	P	300–364	50	8	2100	46	11.4
Wb	L	1207–1335	100	16	420	7	45.5
Tr	L	1350–1478	100	16	250	4	22.0
O8	L_{O8-1}	1360–1488	100	16	310	5	6.3
O8	L_{O8-2}	1594.49–1722.49	100	16	310	5	7.4
Total telescope time/total time on source (hr)[e]							92.5/60.4

Notes.
[a] Wb: Westerbork RT-1 25 m, O8: Onsala 25 m, Tr: Toruń 32 m.
[b] Effective bandwidth accounting for RFI and band edges.
[c] From the EVN status page (http://old.evlbi.org/user_guide/EVNstatus.txt).
[d] Using Equation (1), assuming a 7σ detection threshold and a pulse width of 1 ms.
[e] Total time on source accounts for overlap between the participating stations.

of about 90 ms. The light curve is shown in Figure A1. We assume a spectrum described by thermal bremsstrahlung with a temperature of 30 keV, which is commonly used to describe spectra of magnetar bursts (e.g., Borghese et al. 2019). The resulting average count rate of 406.6 counts s^{-1} corresponds to a flux of 2.04×10^{-8} erg cm^{-2} s^{-1}. The two bursts detected by NuSTAR (8070231100 #7 and #8) were not visible in the INTEGRAL data. The second burst detected with ISGRI occurred on 2022 October 19 at 15:25:54.037 (UTC), during a time gap in the NuSTAR data. Its fluence and duration were 49 counts (30–150 keV) over 200 ms. The rate of 245.0 counts s^{-1} corresponds to a flux of 1.23×10^{-8} erg cm^{-2} s^{-1}.

4. Quasi-simultaneous Radio Observations

We observed SGR J1935 using three radio telescopes in Europe: the 25 m RT-1 telescope in Westerbork, the Netherlands (Wb), the 25 m telescope in Onsala, Sweden (O8), and the 32 m telescope in Toruń Poland (Tr). Observations were carried out at 1.4 GHz, 1.6 GHz (L band), and 330 MHz (P band); see Table 3 for the observational setup. The source was monitored between 2022 October 15 and 19, for a total of 92.5 hr. This number reduces to 60.4 hr when taking into account the overlap between observations at different telescopes.

4.1. Single Pulse Search

We searched the data for FRB-like emission, applying the custom pipeline described by Kirsten et al. (2021, 2022).

Data are recorded as "raw voltages," also known as baseband data, at each station in .vdif format (Whitney et al. 2010). This format encapsulates dual circular polarization with 2-bit sampling. In order to search the data, we first create Stokes I (full-intensity) `filterbank` files with 8-bit encoding using `digifil`, which is part of DSPSR (van Straten & Bailes 2011). For observations at the L band, the frequency resolution is 125 KHz, and the time resolution of the `filterbank` is 64 μs, with the exception of Tr, which has a time resolution of 8 μs. For the P-band observations, these values are 512 μs and 7.8125 KHz, respectively. We mitigated radio-frequency interference (RFI) by applying a static mask. This mask is manually determined for each station and observational setup by identifying channels affected by RFI. We then searched the data for burst candidates using Heimdall,

setting a S/N threshold of 7.[24] We only searched for bursts within a dispersion measure (DM) range of ± 50 units, with the known DM of SGR J1935 being 332.7206 ± 0.0009 pc cm^{-3} (CHIME/FRB Collaboration et al. 2020). Burst candidates are subsequently classified using the machine-learning classifier FETCH (Agarwal et al. 2020). We use models A & H, and set a probability threshold of 50%. The produced burst candidates were then all manually inspected to determine if they are astrophysical or RFI.

4.2. Search for Pulsed Emission

In an effort to detect pulsed radio emission from SGR J1935, we folded our radio data using the ephemeris derived from the X-ray data (see Section 3.1). Additionally, we also folded individual scans which were coincident with an X-ray burst. Overall, we had six instances of overlap between X-ray burst detections and radio coverage. Four of these instances were covered by multiple radio telescopes simultaneously (see Table A2 for details).

The radio observations are divided into scans, each lasting typically 900 s. We first identified the scan that encompassed an X-ray burst, as well as the scans immediately before and after it, totaling roughly 2700 s of data. We used DSPSR to fold the data based on the ephemeris. Folding was only possible due to the contemporaneous X-ray and radio observations. These folded scans were subsequently combined into a single file using `psradd`. We then created a diagnostic plot using `psrplot` to determine the presence of pulsed emission. We validated this method by applying it to observations of the pulsar J1935+1616.

4.3. Results

No FRB-like bursts were found in the radio observations. This allows us to calculate a completeness threshold. The completeness threshold is the upper limit on the fluence of a burst that falls below the sensitivity of our instruments and can be derived using the radiometer equation,

$$\mathcal{F} = (\text{S/N}) \cdot \frac{T_{\text{sys}}}{G} \cdot \sqrt{\frac{W}{n_{\text{pol}}\Delta\nu}} \quad [\text{Jy ms}] \ , \qquad (1)$$

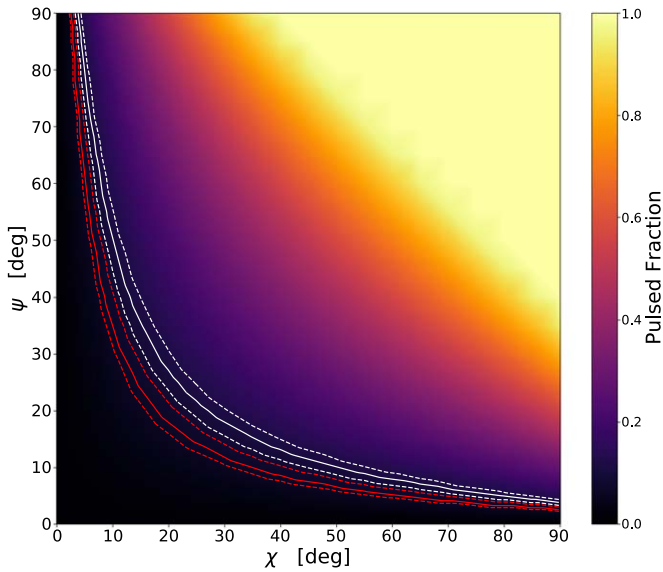[24] https://sourceforge.net/projects/heimdall-astro/

Figure 5. Constraints on the emission geometry of SGR J1935, based on the PF measured in the first epoch (2022 October 15). The color scale represents the 0.3–2 keV PF at different angles. The white lines represent the measured value (PF = 10.8% ± 1.4%), while the red lines represent the measured value at the second epoch (PF = 7.3% ± 1.1%).

where (S/N) is the signal-to-noise ratio detection threshold value, $\frac{T_{sys}}{G}$ is the system-equivalent flux density (SEFD), W is the width of the burst, n_{pol} is the number of recorded polarizations, and $\Delta\nu$ is the recorded bandwidth. Using Equation (1) and the properties of the radio telescopes listed in Table 3, and assuming a width of 1 ms and a 7σ detection threshold, we can find completeness thresholds of 5 Jy ms for Onsala, 4 Jy ms for Toruń 7 Jy ms, and 46 Jy ms for Westerbork in the L and P bands, respectively. Moreover, we folded radio data at the times of overlap between X-ray detections of bursts and we folded all recorded L-band data spread over 4 days from Westerbork and Toruń, which corresponds to 45.5 hr and 21.9 hr of observations, respectively. We found no evidence for pulsed radio emission from SGR J1935 using both approaches. We can therefore determine an upper limit on the typical minimum flux density using the following equation:

$$S_{mean} = (S/N) \cdot \frac{\beta T_{sys}}{G\sqrt{n_{pol}t_{obs}\Delta\nu}} \cdot \sqrt{\frac{W}{P-W}} \ [\text{Jy}] \ , \qquad (2)$$

where β is a factor accounting for quantization effects and is approximated to be 1.1 (see Lorimer & Kramer 2004 and references therein), P is the spin period of the source as quoted in Table 1, and W is the width of the folded profile, which is assumed to be equal to 10% of the period. A complete overview of all derived upper limits can be found in Table A2. For the Westerbork P-band observations, we find a mean flux density limit of 14.86 mJy, while for the L-band observations we find flux density limits between 0.23 and 2.1 mJy for the different telescopes, configurations, and integration times.

5. Discussion

On 2022 October 10–11, the magnetar SGR J1935 entered a new outburst, characterized by the emission of several short X-ray bursts and an increase of the persistent X-ray flux. Moreover, like the previous outburst in 2020, the source emitted a few radio bursts with X-ray counterparts (e.g., Younes et al. 2022a). This event is the sixth detected outburst from SGR J1935, making this magnetar one of the most active known so far.

Here, we presented the properties of the X-ray persistent emission and bursts of SGR J1935 during the first weeks of its most recent outburst based on observations obtained with XMM-Newton and NuSTAR. Additionally, we performed searches for single pulses and pulsed emission through quasi-simultaneous radio observations without any successful results.

Flux and spectral decomposition. The outburst onset was marked by the emission of several short X-ray bursts between 2022 October 10 and 11 (see, e.g., Mereghetti et al. 2022; Palmer 2022). Our observations were carried out ∼6 and 12 days later. At both epochs, emission was detected up to 25 keV (see Figure 4). Hard X-ray emission from SGR J1935 was also seen in a pointing performed ∼5 days after the 2015 outburst onset and was still observed 5 months after the 2020 reactivation (Younes et al. 2017; Borghese et al. 2022). The persistent X-ray spectra were well modeled by the combination of thermal and nonthermal components. The thermal component was well described by a blackbody model. Its parameters remained stable over time, with a temperature of ∼0.4 keV and radius of ∼1.9 km. The nonthermal component had a power-law shape and its contribution to the total 0.5–25 keV luminosity decreased only marginally from ∼93% to ∼89% in about 5 days.

The quiescent level of SGR J1935 is not known yet. Here, we adopt the quiescent observed flux derived by Borghese et al. (2022) using a XMM-Newton observation performed on 2014 October 4, i.e., $(8.7 \pm 0.3) \times 10^{-13}$ erg cm^{-2} s^{-1}(0.3–10 keV). The ratio between the 0.3 and 10 keV observed flux measured during our first observation, $(6.45 \pm 0.05) \times 10^{-12}$ erg cm^{-2} s^{-1}, and that in quiescence is $R_{2022} \sim 7.4$. Assuming the same quiescent flux and considering the peak fluxes of the previous outbursts measured by Younes et al. (2017) and Borghese et al. (2020), we calculated the same ratio. Upon comparison, we found that R_{2022} was greater than the values from the 2014 and 2015 events, which were $R_{2014} \sim 4.9$ and $R_{2015} \sim 5.4$, respectively. However, it was lower than the ratios from the 2016 May and June outbursts, which were $R_{2016\ May} \sim 9.7$ and $R_{2016\ June} \sim 16$, respectively. Notably, the 2020 reactivation was the most powerful, with a ratio of $R_{2020} \sim 49$.

Spin-down rate and pulse profile. We detected the spin period and the spin-down rate using XMM-Newton and NuSTAR data sets, covering the period of 2022 October 15–22. We were able to establish a phase-coherent timing solution (see Table 1). The spin-down rate we inferred was markedly different from those derived during previous outbursts. Specifically, our results indicated that the spin-down rate during the first weeks on the 2022 reactivation ($\dot{P} \simeq 5.52(5) \times 10^{-11}$ s s^{-1}) was a factor of 3.8 times larger than the value measured during the first 4 months of the 2014 outburst ($\dot{P} \simeq 1.43 \times 10^{-11}$ s s^{-1}; Israel et al. 2016), and 1.5 times larger than the spin-down rate during the 2020 outburst ($\dot{P} \simeq 3.5 \times 10^{-11}$ s s^{-1}; Borghese et al. 2022; see also Younes et al. 2020, 2023). The observed variations in the spin-down rate suggest a notable change in the factors affecting the spin-down, e.g., the magnetospheric geometry and/or the relativistic

wind of SGR J1935 during different outbursts. Moreover, changes in the spin-down rate are common during outbursts, indicating changes in the magnetosphere caused by the rearrangement of magnetic fields. To determine the secular spin-down rate of SGR J1935, a targeted monitoring campaign during the quiescence state is needed. The evolution of the pulse profile during the 2022 reactivation of SGR J1935 displays some differences when compared to previous outbursts. The pulse profiles observed in both XMM-Newton and NuSTAR observations exhibits a distinctive double-peaked morphology (see Figure 3). Notably, the second peak (at phase ~0.7) becomes more prominent at energies above 10 keV for both epochs. The observed double-peaked structure contrasts with the quasi-sinusoidal shape showed during the 2014 outburst, as reported in XMM-Newton and Chandra observations (Israel et al. 2016). However, it closely resembles that extracted from NuSTAR and XMM-Newton observations taken during the 2020 outburst (Borghese et al. 2020, 2022). The change of the pulse profile from a single-peak shape in the 2014 outburst to a double-peak shape during the 2022 reactivation may be related to the fact that different regions on the neutron star surface are heated during each outburst. Similarly to the 2014 outburst, we detected an energy-dependent pulse profile phase shift. Slight phase shifts between the peak emissions in the soft and hard X-ray pulse profiles have been observed in a number of magnetars, e.g., XTE J1810 −197 (Borghese et al. 2021) and 1E 1547.0−5408 (see Coti Zelati et al. 2020 and references therein). This phenomenology is consistent with the widely accepted scenario that magnetars' nonthermal X-ray emission stems from resonant inverse-Compton scattering of photons emitted from the star surface by charged particles moving along magnetic loops anchored to the crust and corotating with the star (see Wadiasingh et al. 2018 and references therein). In this scenario, the hard, nonthermal X-ray emission is expected to be beamed along the loop and to be misaligned (in most cases) to some extent with respect to the soft, thermal X-ray emission pattern from the hot spots on the star surface. The PF increased when shifting from the 10–25 keV to 25–79 keV energy bands at each epoch. We also observed a time-dependent change in the PF for the 25–79 keV and 3–25 keV energy intervals, with its value increasing between the two epochs. These results are inconsistent with the findings reported by Israel et al. (2016), where they reported a time-independent PF in the 17%–21% range.

Pulse profile modeling. We determine the emission geometry of SGR J1935 by examining the orientation of the hot spot relative to the line of sight and the star's rotational axis. To achieve this, we compared the observed PF to a set of simulated PFs generated using the method outlined by Perna et al. (2001) and Gotthelf et al. (2010).

Our approach involved creating a temperature map on the surface of the star. This map included a uniform background temperature and a single hot spot characterized by a Gaussian temperature profile. The hot spot's orientation with respect to the star's rotational axis was defined as an angle χ, while we also specified the line of sight's orientation as an angle ψ relative to the rotational axis. We then computed the observed phase-resolved spectra by integrating the local blackbody emission from the visible part of the stellar surface. In this calculation, we considered the effects of gravitational light bending, approximating the

ray-tracing function (Pechenick et al. 1983; Page 1995) using the formula derived by Beloborodov (2002). Additionally, we took into account absorption by the interstellar medium. Since our model includes thermal emission only, we restrict our analysis to the energy range 0.3–2 keV, where the blackbody component dominates the emission. In this range, the PF is $10.8\% \pm 1.4\%$ in the first epoch, and $7.3\% \pm 1.1\%$ in the second one. The pulse profile can be modeled using a simple sinusoidal function with a single peak per rotational phase, so in our modeling we consider a temperature map with a single hot spot. For the temperature and the radius of the hot spot, we considered the values obtained from the phase-resolved spectral fit of peak I reported in Table 2. The contribution from the rest of the stellar surface is neglected since it does not contribute significantly to the emission.

We report the results of our analysis in Figure 5. The color map on the $\chi-\psi$ plane represents the value of the PF obtained by our modeling using the input parameters from the first epoch. The white and red contours represent the regions matching the observed PF in the first and second epoch, respectively. Continuous curves represent the central value of the PF, and dashed curves represent the 1σ uncertainty regions. While the two regions do not overlap, they are consistent within 2σ. Our analysis suggests two preferable configurations: one where both angles have moderate values (e.g., $(\chi-\psi) \sim (25°-25°)$) and another where the line of sight is near the rotational axis and the hot spot is almost perpendicular to it.

radio telescope operated by the Institute of Astronomy of the Nicolaus Copernicus University in Toruń (Poland) and supported by a Polish Ministry of Science and Higher Education SpUB grant.

Facilities: XMM, NuSTAR, INTEGRAL, WSRT, OSO:25m, NCU:TR4.

Software: HEASoft (v6.31; NASA High Energy Astrophysics Science Archive Research Center 2014), FTOOLS (v6.27; Blackburn 1995), XSPEC (v12.3.0; Arnaud 1996), NuSTARDAS (v1.9.2; https://heasarc.gsfc.nasa.gov/docs/nustar/analysis/), NICERsoft packag (https://github.com/paulray/NICERsoft), MATPLOTLIB (v3.6.2; Hunter 2007), NUMPY (v1.23.5; Harris et al. 2020), SAS (v20.0; Gabriel et al. 2004), TEMPO (Nice et al. 2015).

Appendix
Log of Short X-Ray Bursts

Table A1 lists the epochs, fluence, durations, best-fit spectral parameters, and unabsorbed fluxes for the bursts detected in our data sets. The fluence refers to the 3–79 keV and 0.2–12 keV ranges for NuSTAR and XMM-Newton bursts, respectively. The duration has to be considered as an approximate value. We estimated it by summing the 15.625 ms time bins showing enhanced emission for the structured bursts, and by setting it equal to the coarser time resolution at which the burst is detected in all the other cases. Figure A1 shows the light curve of the strongest burst from XMM-Newton, NuSTAR, and INTEGRAL. We also presented the X-ray bursts covered by radio observations in Table A2.

Table A1
Log of X-Ray Bursts Detected in All Data Sets and Results of the Spectral Analysis for the Brightest Events

Instrument/Obs.ID[a]	Burst Epoch YYYY-MM-DD hh:mm: ss (TDB)	Fluence (counts)	Duration (ms)	kT_{BB} (keV)	R_{BB} (km)	$F_{X,unabs}$[b] ($\times 10^{-9}$ erg cm^{-2} s^{-1})	χ^2/ W-stat (dof)
XMM/0902334101 #1[c]	2022-10-15 20:26:14.457	17	31.25	⋯	⋯	⋯	⋯
#2[c]	2022-10-16 00:41:42.870	11	62.5	⋯	⋯	⋯	⋯
#3[d]	03:53:09.083	55	109.375	1.5 ± 0.2	$3.0^{+0.8}_{-0.6}$	0.9 ± 0.1	χ^2=15.86 (14)
#4	10:35:28.285	31	62.5	$1.7^{+0.7}_{-0.4}$	$7.6^{+5.2}_{-2.4}$	10 ± 3	W-stat=21.55 (11)
#5	10:45:11.000	10	62.5	⋯	⋯	⋯	⋯
#6	10:45:14.351	61	109.375	$2.2^{+0.8}_{-0.5}$	$4.6^{+2.1}_{-1.2}$	9 ± 2	χ^2=5.14 (6)
#7	12:05:02.934	29	62.5	$1.4^{+0.4}_{-0.2}$	$7.7^{+3.7}_{-2.0}$	5 ± 1	W-stat=13.54 (16)
NuSTAR/80702311002 #1	2022-10-19 06:29:29.769	25	46.875	⋯	⋯	⋯	⋯
#2	07:56:58.869	13	125	⋯	⋯	⋯	⋯
#3	08:21:05.061	8	62.5	⋯	⋯	⋯	⋯
#4	09:48:56.934	21	46.875	⋯	⋯	⋯	⋯
#5[c]	11:33:02.606	20	46.875	⋯	⋯	⋯	⋯
#6[c]	13:21:31.841	30	62.5	⋯	⋯	⋯	⋯
#7[c]	17:24:38.512	12	31.25	⋯	⋯	⋯	⋯
#8[c]	17:46:13.429	15	125	⋯	⋯	⋯	⋯
#9	2022-10-20 00:13:17.634	80	171.875	$3.1^{+0.6}_{-0.4}$	$1.0^{+0.8}_{-0.6}$	1.2 ± 0.2	W-stat=10.87 (17)
XMM/0882184001 #1	2022-10-22 03:59:47.011	16	62.5	⋯	⋯	⋯	⋯
#2	04:27:31.542	9	31.25	⋯	⋯	⋯	⋯
#3	04:46:13.754	110	218.75	$2.2^{+0.4}_{-0.3}$	$3.9^{+1.0}_{-0.7}$	5.9 ± 0.8	χ^2=4.15 (6)
#4	04:53:17.448	20	62.5	⋯	⋯	⋯	⋯
#5	05:01:16.104	14	62.5	⋯	⋯	⋯	⋯
#6	06:12:48.464	20	125	⋯	⋯	⋯	⋯
#7	06:18:35.417	28	93.75	$2.6^{+1.8}_{-0.7}$	$3.2^{+2.3}_{-1.1}$	7 ± 2	W-stat=14.42 (13)
#8	09:29:20.325	27	93.75	$1.9^{+0.7}_{-0.4}$	$4.9^{+2.9}_{-1.4}$	6 ± 2	W-stat=11.01 (14)
#9	10:01:26.472	132	187.5	$2.3^{+0.6}_{-0.4}$	$4.0^{+1.4}_{-0.9}$	7 ± 1	χ^2=7.33 (6)
#10	14:18.57.919	27	125	$1.4^{+0.4}_{-0.3}$	$3.1^{+1.8}_{-0.8}$	0.8 ± 0.2	χ^2=2.74 (4)
#11	15:41:35.417	12	62.5	⋯	⋯	⋯	⋯
#12	16:25:01.920	30	156.25	$2.4^{+1.2}_{-0.6}$	$2.9^{+1.7}_{-0.9}$	4 ± 1	W-stat=13.08 (18)
#13	16:31:33.816	123	203.125	$1.9^{+0.3}_{-0.2}$	$4.8^{+1.3}_{-0.9}$	5.3 ± 0.7	χ^2=14.13 (8)
#14	16:42:44.030	28	125	$0.8^{+0.2}_{-0.1}$	$12.9^{+8.0}_{-3.7}$	1.5 ± 0.4	W-stat=4.91 (8)
#15	17:37:26.814	290	531.25	2.1 ± 0.2	$3.4^{+0.5}_{-0.4}$	4.0 ± 0.3	χ^2=21.87 (24)
NuSTAR/80702311004 #1	2022-10-22 22:57:23.582	23	62.5	⋯	⋯	⋯	⋯
#2	2022-10-23 21:58:05.838	10	62.5	⋯	⋯	⋯	⋯
#3	22:50:23.135	27	62.5	⋯	⋯	⋯	⋯

Notes. The N_H has been fixed to the average value in the spectral fits.
[a] The notation #N corresponds to the burst number in a given observation.
[b] The flux was estimated in the 0.5–10 keV range for XMM-Newton and NuSTAR.
[c] These bursts were covered by radio observations (for details, see Table A2).
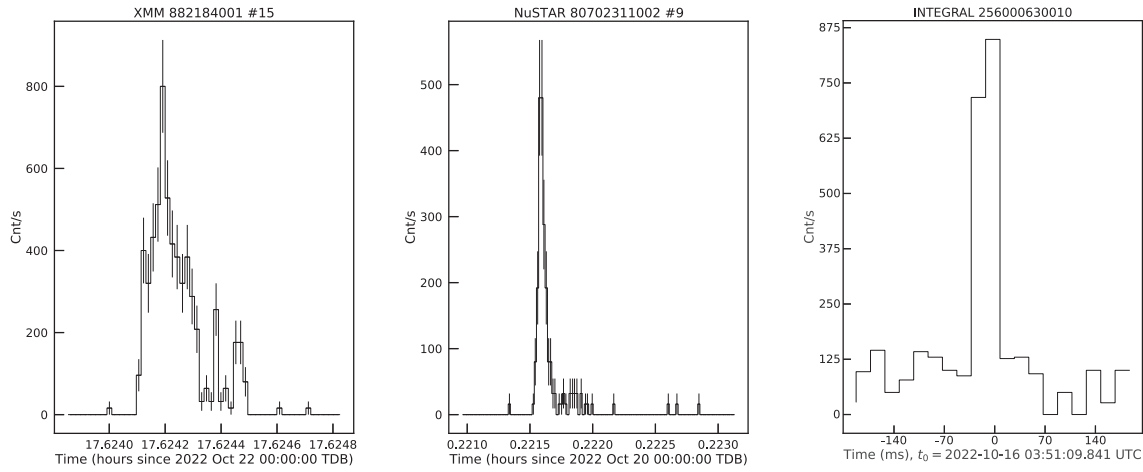[d] Burst detected also with INTEGRAL.

Figure A1. Light curves extracted from XMM-Newton/EPIC-pn (left panel) and NuSTAR/FPMA+FPMB (middle panel) data for the strongest bursts, binned at 62.5 ms, while INTEGRAL/IBIS/ISGRI (right panel) data are binned at 20 ms.

Table A2
Limits on the Mean Flux Density S_{mean} after Folding the Radio Data for the Entire Westerbork and Toruń Observations Using the Ephemeris as Derived in the X-Ray Analysis

Overlap X-Ray	Station	Band	Start Time[a] (TOPO UTC)	Stop Time[a] (TOPO UTC)	#Scans	Exposure Time (s)	S_{mean}[b] (mJy)
	Tr	L	2022-10-15 14:30:08	2022-10-19 22:11:59	111	79041	0.23
	Wb	L	2022-10-16 11:30:41	2022-10-19 23:14:38	180	163754	0.27
XMM/0902334101 #1	Wb	P	2022-10-15 20:13:19	2022-10-15 20:58:38	3	2685	14.86
#1	O8	L_{O8-2}	2022-10-15 20:19:37	2022-10-15 21:04:58	3	2685	1.55
#1	Tr	L	2022-10-15 20:12:57	2022-10-15 20:49:49	3	2138	1.40
#2	O8	L_{O8-1}	2022-10-16 00:24:14	2022-10-16 00:54:21	2	1791	1.90
NuSTAR/80702311002 #5	Wb	L	2022-10-19 11:18:42	2022-10-19 12:04:04	3	2690	2.10
#6	Wb	L	2022-10-19 13:00:50	2022-10-19 13:46:10	3	2687	2.10
#7	Wb	L	2022-10-19 17:04:03	2022-10-19 17:49:24	3	2690	2.10
#7	Tr	L	2022-10-19 17:12:37	2022-10-19 17:49:29	3	2137	1.40
#8	Wb	L	2022-10-19 17:34:27	2022-10-19 18:19:48	3	2691	2.10
#8	Tr	L	2022-10-19 17:37:38	2022-10-19 18:14:30	3	2136	1.40

Notes. Additionally, we also fold and place upper limits on the flux density in the case of X-ray burst overlap instances.
[a] The time elapsed between start and stop times is not continuous due to ∼10 s gaps between scans.
[b] Using Equation (2), properties from Table 3, and assuming a 10σ detection and 10% duty cycle.

ORCID iDs

A. Y. Ibrahim ⓘ https://orcid.org/0000-0002-5663-1712
A. Borghese ⓘ https://orcid.org/0000-0001-8785-5922
F. Coti Zelati ⓘ https://orcid.org/0000-0001-7611-1581
E. Parent ⓘ https://orcid.org/0000-0002-0430-6504
A. Marino ⓘ https://orcid.org/0000-0001-5674-4664
O. S. Ould-Boukattine ⓘ https://orcid.org/0000-0001-9381-8466
N. Rea ⓘ https://orcid.org/0000-0003-2177-6388
S. Ascenzi ⓘ https://orcid.org/0000-0001-5116-6789
D. P. Pacholski ⓘ https://orcid.org/0009-0001-3911-9266
S. Mereghetti ⓘ https://orcid.org/0000-0003-3259-7801
G. L. Israel ⓘ https://orcid.org/0000-0001-5480-6438
A. Tiengo ⓘ https://orcid.org/0000-0002-6038-1090
A. Possenti ⓘ https://orcid.org/0000-0001-5902-3731
M. Burgay ⓘ https://orcid.org/0000-0002-8265-4344
R. Turolla ⓘ https://orcid.org/0000-0003-3977-8760
S. Zane ⓘ https://orcid.org/0000-0001-5326-880X
P. Esposito ⓘ https://orcid.org/0000-0003-4849-5092
D. Götz ⓘ https://orcid.org/0000-0001-9494-0981

S. Campana ⓘ https://orcid.org/0000-0001-6278-1576
F. Kirsten ⓘ https://orcid.org/0000-0001-6664-8668
M. P. Gawroński ⓘ https://orcid.org/0000-0003-4056-4903
J. W. T. Hessels ⓘ https://orcid.org/0000-0003-2317-1446

References

Agarwal, D., Aggarwal, K., Burke-Spolaor, S., Lorimer, D. R., & Garver-Daniels, N. 2020, MNRAS, 497, 1661
Archibald, R. F., Kaspi, V. M., Tendulkar, S. P., & Scholz, P. 2016, ApJL, 829, L21
Arnaud, K. A. 1996, in ASP Conf. Ser. 101, Astronomical Data Analysis Software and Systems V, ed. G. H. Jacoby & J. Barnes (San Francisco, CA: ASP), 17
Beloborodov, A. M. 2002, ApJL, 566, L85
Blackburn, J. K. 1995, in ASP Conf. Ser. 77, Astronomical Data Analysis Software and Systems IV, ed. R. A. Shaw, H. E. Payne, & J. J. E. Hayes (San Francisco, CA: ASP), 367
Bochenek, C. D., Ravi, V., Belov, K. V., et al. 2020, Natur, 587, 59
Borghese, A., Coti Zelati, F., Israel, G. L., et al. 2022, MNRAS, 516, 602
Borghese, A., Coti Zelati, F., Rea, N., et al. 2020, ApJL, 902, L2
Borghese, A., Rea, N., Turolla, R., et al. 2019, MNRAS, 484, 2931
Borghese, A., Rea, N., Turolla, R., et al. 2021, MNRAS, 504, 5244

CHIME/FRB Collaboration, Andersen, B. C., Bandura, K. M., et al. 2020, Natur, 587, 54
Coti Zelati, F., Borghese, A., Rea, N., et al. 2020, A&A, 633, A31
Coti Zelati, F., Rea, N., Pons, J. A., Campana, S., & Esposito, P. 2018, MNRAS, 474, 961
Duncan, R. C., & Thompson, C. 1992, ApJL, 392, L9
Esposito, P., Rea, N., & Israel, G. L. 2021, in Magnetars: A Short Review and Some Sparse Considerations, ed. T. M. Belloni, M. Méndez, & C. Zhang (Berlin: Springer), 97
Gabriel, C., Denby, M., Fyfe, D. J., et al. 2004, in ASP Conf. Ser. 314, Astronomical Data Analysis Software and Systems (ADASS) XIII, ed. F. Ochsenbein, M. G. Allen, & D. Egret (San Francisco, CA: ASP), 759
Gavriil, F. P., Kaspi, V. M., & Woods, P. M. 2004, ApJ, 607, 959
Gehrels, N., Chincarini, G., Giommi, P., et al. 2004, ApJ, 611, 1005
Gotthelf, E. V., Perna, R., & Halpern, J. P. 2010, ApJ, 724, 1316
Harris, C. R., Millman, K. J., van der Walt, S. J., et al. 2020, Natur, 585, 357
Harrison, F. A., Craig, W. W., Christensen, F. E., et al. 2013, ApJ, 770, 103
Hunter, J. D. 2007, CSE, 9, 90
Ibrahim, A. Y., Parent, E., Sathyaprakash, R., et al. 2022, ATel, 15745, 1
Israel, G. L., Esposito, P., Rea, N., et al. 2016, MNRAS, 457, 3448
Kaspi, V. M., & Beloborodov, A. M. 2017, ARA&A, 55, 261
Kirsten, F., Marcote, B., Nimmo, K., et al. 2022, Natur, 602, 585
Kirsten, F., Snelders, M. P., Jenkins, M., et al. 2021, NatAs, 5, 414
Kozlova, A. V., Israel, G. L., Svinkin, D. S., et al. 2016, MNRAS, 460, 2008
Li, C. K., Lin, L., Xiong, S. L., et al. 2021, NatAs, 5, 378
Lin, L., Göğüş, E., Roberts, O. J., et al. 2020, ApJL, 902, L43
Lorimer, D. R., & Kramer, M. 2004, Handbook of Pulsar Astronomy, Vol. 4 (Cambridge: Cambridge Univ. Press)
Luo, J., Ransom, S., Demorest, P., et al. 2021, ApJ, 911, 45
Maan, Y., Leeuwen, J. v., Straal, S., & Pastor-Marazuela, I. 2022, ATel, 15697, 1
Mereghetti, S., Gotz, D., Ferrigno, C., et al. 2022, GCN, 32698, 1
Mereghetti, S., Savchenko, V., Ferrigno, C., et al. 2020, ApJL, 898, L29
NASA High Energy Astrophysics Science Archive Research Center, 2014 HEAsoft: Unified Release of FTOOLS and XANADU, Astrophysics Source Code Library, ascl:1408.004
Nice, D., Demorest, P., Stairs, I., et al., 2015 empo: Pulsar timing data analysis, Astrophysics Source Code Library, ascl:1509.002
Page, D. 1995, ApJ, 442, 273
Palmer, D. M. 2022, ATel, 15667, 1
Pearlman, A. B. & Chime/FRB Collaboration 2022, ATel, 15792, 1
Pechenick, K. R., Ftaclas, C., & Cohen, J. M. 1983, ApJ, 274, 846
Perna, R., Heyl, J., & Hernquist, L. 2001, ApJ, 553, 809
Rea, N., Borghese, A., Esposito, P., et al. 2016, ApJL, 828, L13
Rea, N., Esposito, P., Turolla, R., et al. 2010, Sci, 330, 944
Ridnaia, A., Svinkin, D., Frederiks, D., et al. 2021, NatAs, 5, 372
Stamatikos, M., Malesani, D., Page, K. L., & Sakamoto, T. 2014, GCN, 16520, 1
Strüder, L., Briel, U., Dennerl, K., et al. 2001, A&A, 365, L18
Tavani, M., Casentini, C., Ursi, A., et al. 2021, NatAs, 5, 401
Turner, M. J. L., Abbey, A., Arnaud, M., et al. 2001, A&A, 365, L27
Turolla, R., Zane, S., & Watts, A. L. 2015, RPPh, 78, 116901
van Straten, W., & Bailes, M. 2011, PASA, 28, 1
Verner, D. A., Ferland, G. J., Korista, K. T., & Yakovlev, D. G. 1996, ApJ, 465, 487
Wadiasingh, Z., Baring, M. G., Gonthier, P. L., & Harding, A. K. 2018, ApJ, 854, 98
Whitney, A., Kettenis, M., Phillips, C., & Sekido, M. 2010, in Sixth International VLBI Service for Geodesy and Astronomy, ed. D. Behrend, K. D. Baver et al. (Washington, DC: NASA), 192
Wilms, J., Allen, A., & McCray, R. 2000, ApJ, 542, 914
Younes, G., Baring, M. G., Harding, A. K., et al. 2023, NatAs, 7, 339
Younes, G., Burns, E., Roberts, O. J., et al. 2022a, ATel, 15794, 1
Younes, G., Enoto, T., Hu, C.-P., et al. 2022b, ATel, 15674, 1
Younes, G., Güver, T., Kouveliotou, C., et al. 2020, ApJL, 904, L21
Younes, G., Kouveliotou, C., Jaodand, A., et al. 2017, ApJ, 847, 85
Zhou, P., Zhou, X., Chen, Y., et al. 2020, ApJ, 905, 99